https://doi.org/10.5194/egusphere-2025-446
Preprint. Discussion started: 8 April 2025

Elemental composition, iron mineralogy and solubility of anthropogenic and natural mineral dust aerosols in Namibia: a case study analysis from the AEROCLO-sA campaign

Paola Formenti[1*], Chiara Giorio[2,3], Karine Desboeufs[1], Alexander Zherebker[2], Marco Gaetani[4], Clarissa Baldo[5], Gautier Landrot[6], Simona Montebello[2,7], Servanne Chevaillier[1], Sylvain Triquet[1], Guillaume Siour[5], Claudia Di Biagio[1], Francesco Battaglia[1], Jean-François Doussin[5], Anais Feron[1,$], Andreas Namwoonde[8], and Stuart Piketh[9]

[1] Université Paris Cité and Univ. Paris Est Creteil, CNRS, LISA, F−75013 Paris, France
[2] Yusuf Hamied Department of Chemistry, University of Cambridge, Lensfield Road, Cambridge, CB2 1EW, United Kingdom
[3] Dipartimento di Scienze Chimiche, Università degli Studi di Padova, 35131 Padova, Italy
[4] Classe di Scienze Tecnologie e Società, Scuola Universitaria Superiore IUSS, 27100, Pavia, Italia
[5] Univ Paris Est Creteil and Université Paris Cité, CNRS, LISA, F−94010 Créteil, France
[6] Synchrotron SOLEIL, L'Orme des Merisiers, Saint-Aubin, France
[7] Department of Engineering 'Enzo Ferrari', University of Modena and Reggio Emilia, 41125 Modena, Italy
[8] Sam Nujoma Marine and Coastal Resources Research Centre, University of Namibia, Henties Bay, Namibia
[9] NorthWest University, Potchefstroom, South Africa
[$] now at INRAE

*Correspondence to: paola.formenti@lisa.ipsl.fr

Abstract

This paper presents the results of three weeks of aerosol sampling at the Henties Bay coastal site in Namibia during the Aerosols, Radiation and Clouds in southern Africa (AEROCLO-sA) field campaign in August-September 2017. The campaign coincided with a transition period between two synoptic regimes and corresponded to a significant change in the aerosol composition measured at the site and in particular of that of mineral dust. During August, the dust was natural windblown from the southerly gravel plains with a composition consistent with that previously observed in Namibia. In September, the dust was fugitive from anthropogenic mining and possibly minor contribution of smelting emissions in northern Namibia or as far as the Copper Belt in Zambia, one of the regional hotspot of pollution.

https://doi.org/10.5194/egusphere-2025-446
Preprint. Discussion started: 8 April 2025

Chemical analysis of filter samples highlights the difference in elemental composition, in particular heavy metals, such as As, Cu, Cd, Pb, and Zn, but also silicon, in the anthropogenic dust. The metal solubility of the natural dust was higher, including that of iron. In addition to the higher content of iron oxides and the larger size of particles in the anthropogenic dust, we found that the iron solubility, and, more in general, the metals' solubility, correlated to the high concentrations of fluoride ion which are attributed to marine emissions from the Namibian shelf. These results highlight in a renewed manner the importance of ocean-atmosphere exchanges affecting both the atmospheric composition and the marine biogeochemistry in the Benguela region.

1 Introduction

Mineral dust is an abundant component of the global atmosphere (Kok et al., 2023). Dust particles in the atmosphere are released by the natural wind erosion of natural arid and semi-arid areas of the globe. However, global dust emissions are also contributed by anthropogenic activities such as labouring of bare soils for agriculture, pasture or construction, but also fugitive dust from mining and road traffic activities (Knippertz and Stuut, 2014). Mineral dust is a strong regulator of the Earth's climate and environment (Kok et al., 2023). In the atmosphere, it contributes to both the direct and indirect radiative effects on climate by scattering and absorbing solar and terrestrial radiation and forming cloud droplets in the liquid and ice phases (Kok et al., 2023). It also affects the atmospheric composition and oxidative capacity by acting as a source or a reactive sink of species from the gas phase (Usher et al., 2003). It also acts as an irritating agent for the upper respiratory system and a vector of bacteria and infections (Adebiyi et al., 2023). By deposition, mineral dust can provide nutrients and pollutants to the sea water, changing the ocean's primary production (Knippertz and Stuut, 2014).

These considerations apply to the west coast of southern Africa, and Namibia in particular, a hyper-arid climate where many dust sources co-exist (Vickery et al., 2013). Natural mineral dust is emitted from coastal riverine sources, salty pans such as the Etosha and large gravel plains ubiquitous around the country (Vickery et al., 2013; Dansie et al., 2017; Von Holdt et al., 2018; Klopper et al., 2020; Shikwambana and Kganyago, 2022; Desboeufs et al., 2024). These sources are active throughout the year as emissions occur under various wind regimes (Von Holdt et al., 2018). Natural mineral dust from Namibia is transported within the shallow boundary layer but being able to reach as far as Eastern Antarctica through long-range transport (Gili et al., 2022). Previous research in Namibia has shown that natural mineral dust from the coastal riverbeds and the gravel plains might contribute to oceanic productivity, particularly along the coast (Dansie et al., 2022). This research also pointed to iron as a highly soluble element in both the soil and windblown aerosol fraction and the control for the impact of dust on oceanic productivity (Dansie et al., 2017a; 2017b; 2018; Desboeufs et al., 2024).

https://doi.org/10.5194/egusphere-2025-446
Preprint. Discussion started: 8 April 2025

Furthermore, coastal pollution is an emerging issue of the present-day world (Strain et al., 2022). Increased human activities and coastal developments are quickly affecting the air quality but also the aquatic environment and biodiversity (Micella et al., 2024). Indeed, and despite its low population, Namibia also has intense and emerging economic activities such as mining (various heavy elements, including uranium; Mileusnić et al., 2014; Sracek, 2015; Liebenberg-Enslin et al., 2020) and marine traffic transporting merchandise along the coast of Africa and towards South America (Tournadre, 2014; Klopper et al., 2020). These activities release fugitive dust from the mine locations as well as from the numerous road constructions from and to the major national harbour, Walvis Bay (https://mwt.gov.na/projects; last accessed 26/11/2024). In Namibia, the accumulation of heavy metals in the shore and coastal waters due to coastal mining (Onjefu et al., 2020) has been previously documented (Sylvanus et al., 2016; Omoregie et al., 2019; Nekhoroshkov et al., 2021). Furthermore, in the austral wintertime, Namibia is affected by anti-cyclonic circulation, resulting in the transport of light-absorbing particles, likely from forest fires and mining areas such as the Zambian Copper Belt (Formenti et al., 2018; Aurélien et al., 2022; Martinez-Alonso et al., 2023; Kříbek et al., 2023). The composition of these emissions is little characterised to date while having the potential for alter the oceanic productivity and microbial biogeochemistry (Adriano, 2001; Jordi et al., 2012; Mahowald et al., 2018; Yang et al. 2019).

In this paper, we present a case study analysis of the differences and similarities of the composition of natural and anthropogenic mineral dust sampled during the ground-based field campaign of the Aerosols, Radiation and Clouds in southern Africa (AEROCLO-sA) project (Formenti et al., 2019). The campaign was conducted in August-September 2017 in Henties Bay (22°6′S, 14°30′E; 20 m above mean sea level) along the Namibian coast.

Based on analysis of the chemical composition and meteorological fields, we demonstrate the origin of the anthropogenic dust and contrast its elemental composition, iron mineralogy and solubility, and the type of organic matter with respect to that of natural dust measured at the beginning of the campaign. Our analysis focusses on the iron mineralogy and solubility but includes, for the first time the evaluation of the solubility of heavy metals transported with these emissions.

2 Experimental

The AEROCLO-sA field campaign took place from 21 August to 13 September 2017 at the Sam Nujoma Marine and Coastal Resources Research Centre (SANUMARC) of the University of Namibia at Henties Bay (Formenti et al., 2019). This sampling site, operated on the long-term as described by Formenti et al. (2018) and Klopper et al. (2020), was augmented with the

https://doi.org/10.5194/egusphere-2025-446
Preprint. Discussion started: 8 April 2025

PortablE Gas and Aerosol Sampling UnitS (PEGASUS; https://pegasus.aeris-data.fr/; last accessed 24/01/2025) mobile facility for the time of the campaign.

The PEGASUS facility consists of two marine containers (20-feet long) customized and equipped for atmospheric research (Formenti et al., 2019). Air sampling is performed with two high-volume aerosol inlets delivering approximately 450 L min^{-1} each. At wind speeds between 5 to 10 m s^{-1}, typical for coastal Namibia (see Figure S1), sampling is almost isokinetic for particles up to 40 µm in aerodynamic diameter (Rajot et al., 2008), which hereafter we named total suspended particulate (TSP). The total sampled flow rate is distributed to online analysers and to multiple- and single-stack sample collection units for off-line analysis of the bulk and size-resolved chemical and mineralogical composition, soluble fraction and mixing state. The details of the online instrumentation relevant to this publication are listed in Table S1 in the supplementary material.

2.1 Sample collection

During the campaign, aerosol samples were collected both during day (approximately 07:00-17:00 UTC) and night time (approximately 17:30-06:30 UTC). The sampling duration was marginally adapted in real-time to the nature and the aerosol load of air masses using the readings of the local wind speed and direction and of the aerosol mass concentration, also measured online.

Four custom-made filter holders were used in parallel for collecting aerosols in the TSP fraction. These were loaded with (i) one Teflon filter (Zefluor®, 2-µm pore size diameter, 47-mm filter diameter); (ii) two polycarbonate membranes (Nuclepore®, 0.4-µm pore size diameter, 37-mm and 47-mm filter diameter, respectively), and (iii) a quartz filter (Pall, 2500QAT-UP Tissuquartz, 47-mm filter diameter). The average sampling flow rate varied between 20 and 30 L min^{-1}.

Two samples of the composition of particles smaller than 1 µm in diameter (hereafter named PM_1 size fraction) were collected in parallel using two 4-stage Dekati® PM_{10} Impactors, both operated at 10 L min^{-1}. For these two samplers we used 25-mm polycarbonate membranes on three impactor stages (> 10 µm, 10-2.5 µm and 2.5-1 µm) while the final filter stage, where the PM_1 fraction is collected, was a polycarbonate membrane (Nuclepore®, 0.4-µm pore size, 47-mm filter diameter) and a quartz filter (Pall, 2500QAT-UP Tissuquartz, 47-mm filter diameter), respectively.

Before the campaign, Teflon and quartz membranes were cleaned for sampling organic aerosols. Teflon membranes were rinsed with dichloromethane and baked at 100°C for 10 minutes. Quartz membranes were baked at 550°C for 12 hours. Both were conditioned in pre-baked aluminium foils. The polycarbonate membranes were used for measuring the inorganic

https://doi.org/10.5194/egusphere-2025-446
Preprint. Discussion started: 8 April 2025

and water-soluble fraction composition. The 37-mm and 25-mm membranes were used as purchased, while the 47-mm ones were acid-washed according to the protocol described in Desboeufs et al. (2024). All material was sealed and opened only before collection. Immediately after exposure, all samples were sealed and stored at -18°C in the deep-freezer available in the PEGASUS facility, from which they were transported back to the laboratory.

TSP filter samples were collected between 21 August and 12 September 2017, while PM_1 samples were collected from 26 August 2017 onwards. In total, 36 TSP and 31 PM_1 samples were collected per filter type during the field campaign (including blanks).

2.2 Sample analysis

2.2.1 Elements and water-soluble ions

The analysis of the elemental and water–soluble ion concentrations was performed at LISA according to the protocols previously detailed in Klopper et al. (2020) and Desboeufs et al. (2024). The elemental concentrations of 24 elements (Na, Mg, Al, Si, P, S, Cl, K, Ca, Ti, V, Cr, Mn, Fe, Co, Ni, Cu, Zn, As, Sr, Pb, Nd, Cd, Ba) were measured by wavelength-dispersive X-ray fluorescence (WD-XRF) using a PW-2404 spectrometer (Panalytical, Almelo, Netherlands). The instrument was calibrated with mono- and bi-elemental certified elemental standards (Micromatter Inc., Surrey, Canada). The concentrations of light-weight elements (Na to Ca) in the TSP fraction were corrected for X-ray self-attenuation as described in Formenti et al. (2010), assuming a mean diameter of 4.5 µm to represent the average coarse particle size. Elements heavier than Ca, as well as concentrations measured in the PM_1 fraction, were not corrected. The measured atmospheric concentrations are expressed in ng m^{-3}, and the relative analytical uncertainty was evaluated as 10 %.

The analysis of the water-soluble fraction was performed by extracting the filters with 20 mL of ultrapure water (MilliQ® 18.2 MΩ.cm) for 30 minutes. The solution was divided into two sub-samples filtered to 0.2 µm of porosity (Nuclepore). One half was analyzed by Ion chromatography (IC) using a Metrohm IC 850 device equipped with a column MetrosepA supp 7 (250/4.0 mm) for anions and with a Metrosep C4 (250/4.0 mm) for cations. The IC analysis provided the concentrations of the following water-soluble ions: F^-, formate, acetate, MSA^- (methanesulphonic acid), Cl^-, NO_3^-, SO_4^{2-}, oxalate, Na^+, NH_4^+, K^+, Ca^{2+} and Mg^{2+}. A calibration with certified standard multi-ions solutions of concentrations ranging from 5 to 5000 ppb was performed and, the uncertainty of the analysis was estimated to be 5%.

The second half of the solution was acidified to 1% with ultrapure nitric acid (HNO_3) and analysed by a combination of inductively coupled plasma-atomic emission spectroscopy (ICP

https://doi.org/10.5194/egusphere-2025-446
Preprint. Discussion started: 8 April 2025

AES) using Spectro ARCOS Ametek® ICP-AES and by high-resolution inductively coupled plasma-mass spectrometry (HR-ICP-MS) using a Neptune Plus™ instrument by Thermo Scientific™ as described in Desboeufs et al. (2024). The calibration curve was performed using standard multi-element solutions ranging from 1 to 1000 ppt. The elemental fractional solubility (FS) for element is calculated as the ratio between the dissolved and the total concentration.

Organic carbon (OC) and elemental carbon (EC) were measured using a thermo-optical carbon analyser (Sunset Laboratory Inc.) on a 1.5 cm^2 filter following the EUSSAR-II protocol (Cavalli et al., 2010). The Sunset analyzer was calibrated using a sucrose solution (purity > 99.5 %) in the concentration range between 0.42 µg cm^{-2} and 40 µg cm^{-2}. The limit of quantification for total carbon and organic carbon is henceforth estimated to be equal to 0.42 µg cm^{-2}. An instrumental blank and a control point with a sucrose solution at 10 µg cm^{-2} were done at the beginning of each day of analysis. OC and EC concentrations are automatically calculated with the software OCBC835 (Sunset Laboratory). The optical split point was manually verified to ensure their assignment.

All the concentration values presented in this paper were corrected for the average concentration measured for their corresponding analytical blanks, which was almost equal to the limit of detection.

2.2.2 Iron mineralogy

The quantification of iron oxides and the partitioning of iron species in the II- and III-oxidation state was performed by X-Ray Absorption (XAS) analysis at the Fe K-edge. Analysis was performed on the Teflon TSP filters only as the concentrations of the PM_1 filters were not high enough for this kind of analysis.

XAS analysis was conducted at the SAMBA (Spectroscopies Applied to Materials based on Absorption) line at the SOLEIL synchrotron facility in Saclay, France (Briois et al., 2011) according to the protocols and procedures previously presented in Formenti et al. (2014) and Caponi et al. (2017). A Si(220) double-crystal monochromator was used to produce a monochromatic X-ray beam, which was 4000 x 1000 $µm^2$ in size at the focal point. The energy of the X-ray beam was calibrated with an external Fe foil standard before the experiments. The energy range was scanned from 7050 eV to 7350 eV at a step resolution of 0.2 eV.

Aerosol samples were mounted in an external setup. A portion of each aerosol filter sample was cut and mounted on a carton board holder with 5 available positions and analysed in fluorescence mode without prior preparation. The number of scans per sample was set between 50 and 200, depending on the iron concentration, to improve the signal-to-noise ratio. One scan acquisition lasted approximately 100 seconds for a total of 1.3 hours to 5.5 hours of measurements for 50 to 200 scans.

https://doi.org/10.5194/egusphere-2025-446
Preprint. Discussion started: 8 April 2025

The spectral analysis was conducted with the FASTOSH software package developed at SAMBA. As described in Wilke et al. (2001) and O'Day et al. (2004), the oxidation state and the bonding environment of Fe in dust samples give rise to different features in the XAS spectra. In the pre-edge region, the shape of the XAS spectra is determined by electronic transitions to empty bound states, which are strongly influenced by the oxidation state of the absorbing atom but also by the local geometry around the absorbing atom due to hybridization effects. Wilke et al. (2001) found that for Fe(II)-bearing minerals, the position of the centroid of the pre-edge is found at 7112.1 eV, whereas it is at 7113.5 eV for Fe(III)-bearing minerals. The position of the rising edge, which also depends on the oxidation state, is found at approximately 7120 eV. In the X-ray Absorption Near Edge Structure (XANES) region, extending approximately 50 eV above the K-edge peak, features are determined by multiple-scattering resonances of the photo-electron ejected at low kinetic energies.

The speciation of Fe was obtained by the least-square fit of the measured XANES spectra based on the linear combination of mineralogical references. Fits were conducted on the first derivative of the normalized spectral absorbance in the energy region between 7100 to 7180 eV, corresponding to -30 and +50 eV of the K-edge. Only the fits with a χ^2 closest to 1 were retained for further analysis.

The reference standards were chosen based on the expected iron mineralogy in the area (White et al., 2007; Heine and Völkel, 2010; Formenti et al., 2014; Sracek, 2015; Zhang et al., 2022). Standards for clays (illite and montomorrilonite) and iron oxides as goethite, magnetite and hematite were taken from Formenti et al (2014) and Baldo et al. (2020). The ferrihydrite standard was derived by the database of the Advanced Light Source, Lawrence Berkeley National Lab (S. Frakra, pers. comm.). Standards for metal-ligand complexes expected to form in fog droplets and deliquescent aerosol at high RH (Giorio et al., 2022) is provided in Table S2 in the supplementary material.

2.2.3 Organic analysis

The water-soluble fraction of organic aerosols (WSOC) was extracted, purified using hydrophobic resin (Bond Elut ppl) and analysed by high-resolution mass spectrometry (HRMS) namely by hybrid LTQ-Orbitrap equipped with electrospray source (ESI) operated in negative ion mode. All the samples were directly injected into the ESI source using a syringe pump. In each case spectra were recorded in triplicates in two mass diapasons to decrease the number of ions in the detector: 50-500 m/z and 150-700 m/z. Raw spectra were treated following the laboratory procedure reported in Zherebker et al. (2024). Files were converted to *.mzML format using msconvert with vendor-recommended peak-picking algorithm (https://proteowizard.sourceforge.io/; last accessed 18/12/2024), which was suitable for a

https://doi.org/10.5194/egusphere-2025-446
Preprint. Discussion started: 8 April 2025

series of in-house written Python scripts which included de-noising, calibration, formulae assignment, and blank subtraction. Only formulae presented in triplicates were retained. Diapasons were combined with removing lower-intensity duplicates. Formulae assignment was performed considering only single-charged ions, ignoring anion-radicals with the following atomic constraints: O/C ratio ≤ 2, 0.3 < H/C ratio < 2.5; element counts [1 < C ≤ 60, 2< H ≤ 100, 0 < O ≤ 60, N ≤ 2, S ≤ 1]. Each formula was attributed to the tentative chemical class (Table S4) based on the constrained aromaticity index (AI_{con}) calculated according to Zherebker et al. (2022). In addition, the double bond equivalent (DBE) has been calculated, which represents the sum of sp^2 and sp bonds and cycles. Further details of the mass-spectrometry results are provided in Text S1 in the supplementary material.

2.3 Ancillary products

2.3.1 Air mass back trajectories

Three-dimensional air mass back-trajectories ensemble are calculated using the NOAA HYbrid Single-Particle Lagrangian Integrated Trajectory Model (HYSPLIT; Draxler and Rolph, 2015). Weather Research Forecasting Model (WRF, version 3.71; Skamarock et al., 2008) forced by Operational Global Analysis data (NCEP: National Centers for Environmental Prediction; GDAS: Global Data Assimilation System, https://rda.ucar.edu/datasets/d083002, last accessed 10/01/2025) was used to simulated hourly meteorological data at 50km and 9km horizontal resolution.

2.3.2 Atmospheric circulation

The atmospheric circulation and composition at the regional scale from 21 August to 13 September 2017 was further investigated using the Copernicus Atmospheric Monitoring Service (CAMS) reanalysis (Inness et al., 2019), available every 3 h from 00:00 to 21:00 UTC. The spatial resolution is approximately 80 km and 60 pressure levels (37 of which are below 20 km and 20 below 5 km). The atmospheric composition is described by analysing the total aerosol optical depth (AOD) at 550 nm and the mass mixing ratio of dust and sulphate aerosols. The atmospheric circulation is described by analysing the near-surface (10 m) wind, to highlight emission processes and local transport, and the geopotential height at 700 hPa, to highlight the large-scale circulation and long-range transport. Atmospheric composition and circulation data are averaged at the daily time scale.

2.3.3 Positive matrix factorisation analysis

Positive Matrix Factorisation (PMF) (Paatero, 1997; Paatero and Tapper, 1994) was applied to chemical composition data (OC, EC, inorganic ions and total metals) of TSP and PM_1 samples using the software EPA PMF 5.0. Different factor solutions were investigated in the range of 3 to 8 factors, starting from 10 different seeds. The 4-factor solution and the 3-factor

https://doi.org/10.5194/egusphere-2025-446
Preprint. Discussion started: 8 April 2025

solution were selected for TSP and PM_1, respectively, based on the inflexion point of Q/Qexp and chemical interpretation of the resulting factor profiles (loadings). The selected solutions were run again from 100 different seeds, and the solutions with the lowest Q were selected. Rotational ambiguity was investigated by changing the Fpeak parameter from 0 to ± 0.5 and ± 1. The solutions with Fpeak = 0 were selected, and bootstrap analysis was performed using a number of bootstraps of 100 and a minimum r-value of 0.6.

3 Results

3.1 Air mass origin and local meteorology

Chazette et al. (2019) and Gaetani et al. (2021) showed that mid-tropospheric air masses during the field campaign were characterized by three distinct periods. A first period (P1; 22–28 August 2017) when air masses were southerly and characterized by low aerosol content and large particles. From 23 to 25 August, the circulation in the middle troposphere was characterized by the reinforcement of the South Atlantic anticyclone, leading to prevailing south-westerly winds above Namibia (Figure S2). From 26 to 28 August, the transit of a disturbance in the Southern Ocean was accompanied by the installation of the continental high and prevailing north-westerly winds above Namibia (Figure S2). A second period (P2; 29 August–1 September 2017) when the circulation was characterized by the weakening of the South Atlantic anticyclone and the reinforcement of the continental high (Figure S2), associated with a northerly/easterly flow and transport of recirculation of a higher load of aerosols associated with biomass burning. The circulation pattern remained the same on the third period (P3; 3–12 September 2017), but the aerosol content further increased. After the transit of a cut-off low in the upper troposphere on 2-4 September (Flamant et al., 2022), the large-scale circulation was dominated by the further reinforcement of the continental high and, on the 8-9 September, by the installation of a trough over the South Atlantic, leading to favourable conditions for the recirculation of continental aerosol towards Namibia.

The same synoptic circulation was observed at the surface level. Air mass back trajectories (Figure S3) show that the air flow at the surface level was southerly during P1 and P2 but shifted to north-easterly (continental) after 2 September (P3), when the frequency of the anti-cyclonic circulation towards Henties Bay increased. Continental air masses generally took more than 2 days to reach the site. In the last two days of transport, they moved along the coast or recirculated around Henties Bay, alternating the S-SW and NW-NNW directions. In a few cases, and in particular on 11 September, the transport of continental air masses was more direct and within two days from Henties Bay. The record of local winds measured during the campaign (Figure S1 in the supplementary material) testifies of the frequent recirculation. Strong winds (average 5 m s^{-1}, and up to 10 m s^{-1}) came, alternatively, from the S-SW direction

https://doi.org/10.5194/egusphere-2025-446
Preprint. Discussion started: 8 April 2025

(20-22 August, 29-31 August, 6-9 September, 11 September, grey boxes in Figure S1) and the NW-NNW direction (23-28 August, 1-5 September, 10 September, 12-13 September). Occasionally, a gentle land breeze (easterly winds below 2 m s^{-1}) was observed before sunrise or after sunset. In general terms, as discussed in Giorio et al. (2022), the local meteorological conditions at Henties Bay during the campaign were characterized by remarkable stability in terms of temperature (around 12 °C) and humidity (RH ~95%), while a persistent stratocumulus cloud deck kept solar irradiance below 600 W m^{-2}.

3.2 Aerosol composition and origin

The summary statistics of the aerosol composition is reported in Table S3 as supplementary information. The TSP chemical composition was dominated by the sea salt tracers, Na^+ and Cl^- (average ± standard deviation concentrations of 22 ± 11 µg m^{-3} and 39 ± 21 µg m^{-3}, respectively), as well as SO_4^{2-} (9.1 ± 4.3 µg m^{-3}), Mg^{2+} (3.9 ± 2.0 µg m^{-3}), K^+ (1.2 ± 0.6 µg m^{-3}) and Ca^{2+} (1.7 ± 0.8 µg m^{-3}). In terms of metals and metalloids, Al (0.6 ± 0.4 µg m^{-3}), Fe (0.6 ± 0.4 µg m^{-3}), and Si (2.5 ± 1.3 µg m^{-3}) had the highest concentrations. The mean OC and EC concentrations were 3.2 ± 1.5 µg m^{-3} and 0.2 ± 0.2 µg m^{-3}, respectively. The concentrations of methanesulfonic acid (MSA), tracer of marine biogenic productivity, averaged at 61 ± 26 ng m^{-3}. In the PM_1 fraction, due to the low flow rate used for sampling (10 L min^{-1}), only major elements and ions were detected. Concentrations in the PM_1 fraction were generally lower than in the TSP.

3.2.1 Marine aerosols

Figure 1 presents the time series of the elemental concentrations of Na^+ and Cl^- and their ratios (Cl^-/Na^+) in the TSP and PM_1 fractions.

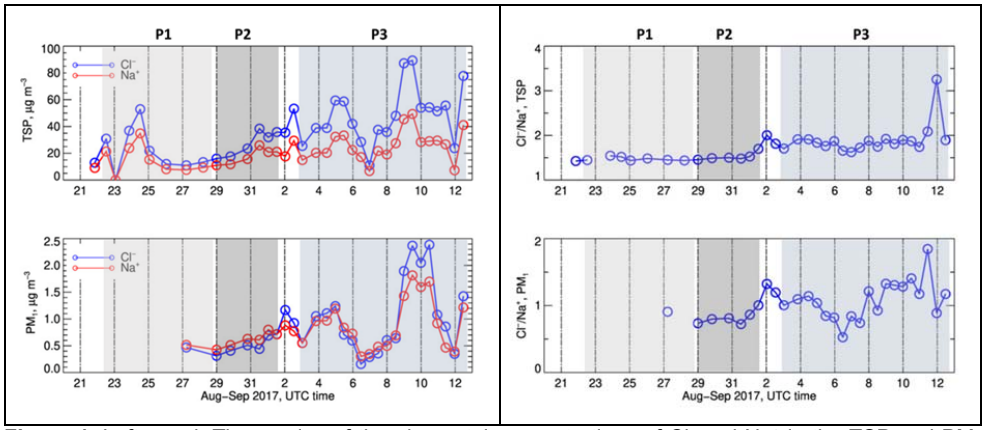

Figure 1. Left panel: Time series of the elemental concentrations of Cl^- and Na^+ in the TSP and PM_1 fractions. Right panel: Time series of elemental ratio of Cl^-/Na^+ in the TSP and PM_1 fractions.

https://doi.org/10.5194/egusphere-2025-446
Preprint. Discussion started: 8 April 2025

The concentrations of Na^+ and Cl^-, strongly correlated as expected, showed a relatively constant background of approximately 10 µg m^{-3} (TSP) and 0.3 µg m^{-3} (PM_1), and intense peaks of concentrations. In the TSP fraction, the Cl^- concentration was up to 80 µg m^{-3}. The Cl^-/Na^+ ratio was of the order of 1.5 in the P1 and P2 periods, and of the order of 1.8 afterwards. In the PM_1 fraction, the Cl^- concentration reached 2.5 µg m^{-3}. The Cl^-/Na^+ ratio, little documented during P1, was around 0.7, while it increased between 1 and 1.8 during P2 and P3. Values of the order of 1.5-1.8 are consistent with the composition of local seawater (Giorio et al., this issue) and average sea spray (Seinfeld and Pandis, 2006), as well as the previous results by Klopper et al. (2020).

The mass concentration of organic carbon (OC) through the campaign was strongly associated with Na^+ as well as Cl^- (not shown). The OC/Na^+ ratio was variable and ranged between 0.07 and 0.3, consistent with values reported by Frossard et al. (2014) for marine aerosol types. The molecular analysis of the organic composition provides insights into the sources affecting the OC/Na^+ ratio during the campaign (Figure 2).

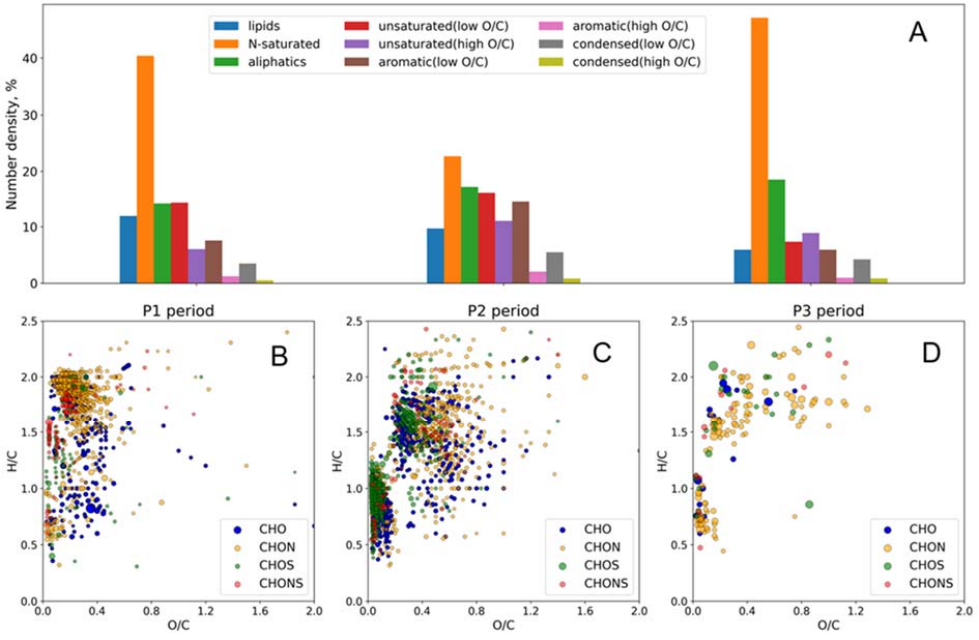

Figure 2. Population density of all molecular compositions based on AIcon classes (a), and van Krevelen diagrams for only unique molecular assignments in samples under study in the three periods (b-d), where unique formulae were determined only in a sample from the designated period. The size of the points reflects relative intensities in the mass spectra (not used in the analysis).

The differences in the molecular composition of samples from the P1-P3 periods are depicted in the van Krevelen diagrams (Figure 2b-d), which highlight the unique molecular composition

https://doi.org/10.5194/egusphere-2025-446
Preprint. Discussion started: 8 April 2025

of each period. P1 was dominated by saturated and low oxidized (O/C < 0.3) CHO and CHON compounds, which occupy about 60% of the total molecular space (Figure 2). This may indicate the high contribution of biogenic fatty acids and protein-derived compounds (Bikkina et al., 2019). Their cumulative contribution in P2 decreased to about 40%, while a significant increase in the contribution of oxidized saturated compounds (O/C > 0.3) as well as highly unsaturated (AI_{con} > 0.5) compounds was observed. Moreover, reduced (low O/C) saturated compounds appear to be unique for the P1 period (Figure 2b). This supports the biogenic source brought by south-westerly winds. Further, the contribution of continental dust with clear anthropogenic contribution is reflected as unique highly unsaturated compounds in the P2 period as well as an increase in S-containing compounds (Figure 2c). P3 was depleted with highly unsaturated compounds with a relative dominance of saturated N-containing compounds. The aerosol sources are similar between the P2 and P3 periods, which resulted in an insignificant amount of unique molecular assignment in the latter (Figure 2d). In addition, the double bond equivalent *vs*. molecular mass diagram in the supplementary material indicates an increase in the contribution of biomass-burning aerosols and possibly sulphate-enriched dust from smelting in the P2-P3 periods compared to the P1 period, which is in line with the air mass origin. Further details of the organic composition are reported in the supplementary materials.

3.2.2 Fluoride concentrations

The P1 and P2 periods were also characterised by extremely high concentrations of fluoride (up to 10 μg m^{-3}) as shown in Figure 3, in line with what reported by Klopper et al. (2020) for the PM_{10} aerosols measured during 2016 and 2017 at the site. In September (P3), the concentration of F^- dropped to zero, as a consequence of the change in the origin of the air masses transported to the site.

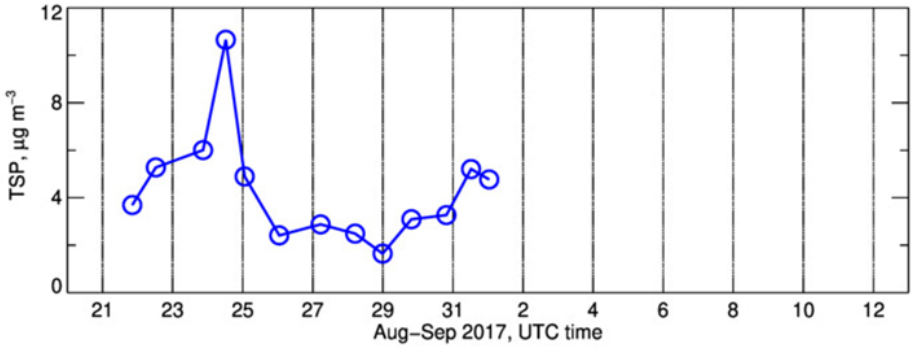

Figure 3. Time series of the elemental concentrations of F^- in the TSP fraction during the field campaign.

https://doi.org/10.5194/egusphere-2025-446
Preprint. Discussion started: 8 April 2025

Fluoride is a natural occurring ion in marine environments as well as in mineral dust (Fuge, 2019). In Namibia, the release of dissolved fluoride to the atmosphere is due to the evaporation of fluoride-rich groundwater (Sracek et al., 2015) or the erosion of mineral deposits of calcium fluoride (CaF_2, Onipe et al., 2020). Fluoride is present in significant amounts (> 1 wt.% F) in francolite, a carbonate fluorapatite mineral (typical formula $Ca_{4.7}Na_{0.2}Mg_{0.1}(PO_4)_{2.6}(CO_3)_{0.4}F_{1.28}$), which can be found in phosphorite deposits on the Namibian shelf, notably in the area between 23° and 25.5°S south of Henties Bay (Compton and Bergh, 2016; Mänd et al., 2018). This is likely to be the origin of the excessive fluoride concentrations observed during the P1 period of the campaign. Not only the origin of air masses detected at Henties Bay coincided with the locations of the marine deposits, but during P1 the fluoride content correlated with major marine tracers (Na, Cl, S), and with calcium, both its sea salt and non-sea-salt fractions (nss-Ca^{2+}/F^- ratio ranging from 0.1 to 0.3, as in Klopper et al. (2020)), as well as with P, K and Sr, the latter can replace Ca in the francolite mineral structure (Compton and Bergh, 2016; Rakovan and Hughes, 2000).

3.2.3 Mineral dust composition

Figure 4 presents the time series of the elemental concentrations of Al, Si and Fe, major tracers of mineral dust, as well as of their ratios (Si/Al, Fe/Al and Fe/Si) in the TSP and PM_1 fractions.

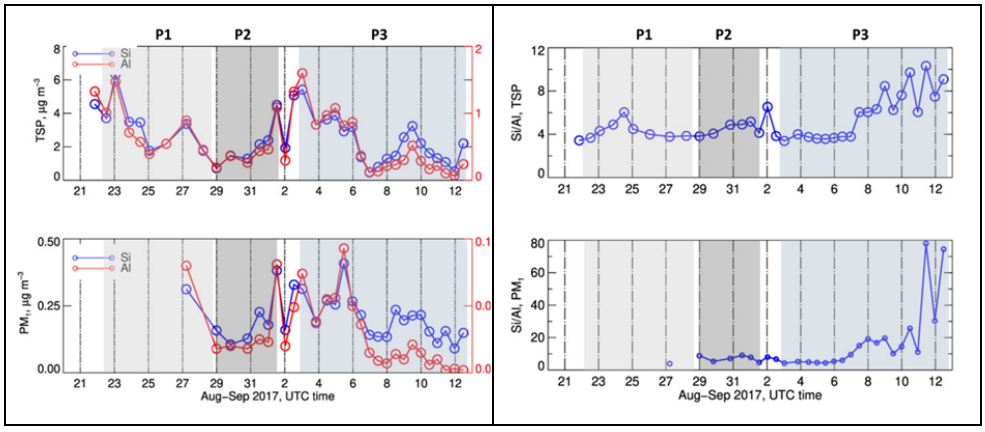

https://doi.org/10.5194/egusphere-2025-446
Preprint. Discussion started: 8 April 2025

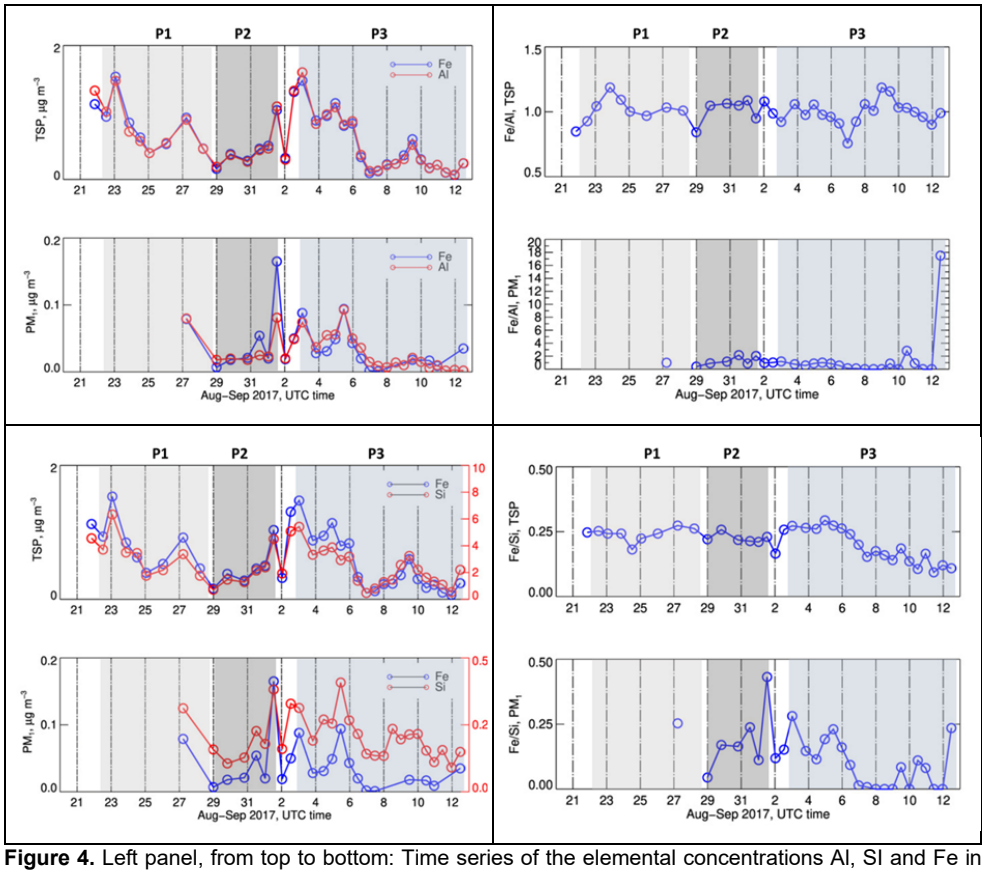

Figure 4. Left panel, from top to bottom: Time series of the elemental concentrations Al, Sl and Fe in the TSP and PM_1 fractions. Right panel from top to bottom: Time series of elemental ratio of Si/Al, Fe/Al and Fe/Si in TSP and PM_1 fractions.

The elemental concentrations of Si and Al were up to 6 and 1 µg m^{-3} in the TSP fraction and up to 410 and 90 ng m^{-3} in the PM_1 fraction, respectively. In the P1 and P2 periods, and with the exception of a peak value on 26 August, the Si/Al ratio was of the order of 3.8, consistent with the findings of Klopper et al. (2020) for natural mineral dust emitted from the Namibian gravel planes. After this date, that is during P3, the Si/Al ratio increased to values between 6 and 10 (TSP) and between 8 and 80 (PM_1), indicating a very strong enrichment with respect to the composition of the regional mineral dust.

In the TSP fraction, and regardless of the period, the Fe/Al ratio was in the range of 0.8-1.2, as previously found for the natural gravel plain dust in the area (Eltayeb et al., 1993; Klopper et al., 2020). Likewise, during P1 and P2 the Fe/Si ratio was consistent with those previous observations for mineral dust, and so was the Fe/Ca ratio (not shown), found in the range 0.2-0.8. However, during P3, the Fe/Si decreased from approximately 0.25 to 0.1, while the Fe/Ca

https://doi.org/10.5194/egusphere-2025-446
Preprint. Discussion started: 8 April 2025

ratio increased to between 0.09-0.15 (not shown). In the PM_1 fraction, both the Fe/Al and the Fe/Si ratios were more variable with time (only the September period is documented). The Fe/Al ratio was of the order of 1 as in the TSP fraction, except on the last day of the campaign when the ratio reached 18. The Fe/Si was higher between 29 August and 6 September (e.g., the P2 period), ranging from 0.2 to 0.4, and decreased to 0.1-0.2 in the last days of the campaign. That corresponded to the variability of several major elements and metals (K, Mg, Co, Cu, Nd, Ni, Sr, Cd, but Zn, As and Pb in particular), whose ratio with Al were significantly higher during the last days of the campaign (7-12 September, Figure S5). As for OC/Na^+, the aerosol mineral composition of TSP during the P3 period could be split into two sub-periods before and after 6 September, with an enrichment in metals and OC at the end of the campaign.

3.2.4 Source apportionment

These observations are reflected by the PMF analysis, described in Text S2 in the supplementary material. Note that, despite its high concentrations, fluoride was not included in the source apportionment because it was not measured during the whole field campaign. In the TSP fraction, the analysis separates two factors characterized by a high loading of metals. The first one is a “mineral dust” factor characterized by Al, Fe, and Si, as well as Ti, Mn, Na^+, Ca^{2+}, and SO_4^{2-}. Its contribution, significant only during the first part of the campaign, accounted, on average, for 5.8% of total TSP mass. The second factor, called “Si-rich”, is characterized by the presence of a high loading of Si, As and Pb, strongly correlated to each other (r=0.97), moderate loadings of Co, Cu, Ni, Nd, Sr, Zn and EC, but not correlated to Al nor Fe, contrarily to “mineral dust”. The “Si-rich” factor, significant mostly during the P3 period, notably after the 6 September, accounted for 23.3% of TSP mass but was not found in the PM_1 fraction where the concentrations of the majority of its tracers were very close to the detection limit. This is in agreement with the fact that the fraction of coarse particles with respect to the total number increased on the last days of the campaign (Figure S6 in the supplementary material).

The chemical fingerprinting of the “Si-rich” factor is similar to that reported from windblown dust from mines in the Otavi Mountainland in Namibia (Mileusnić et al., 2014; Sracek, 2015) as in the Zambian Copper Belt (Meter et al., 1999; Ettler et al., 2011; 2014; Mwaanga et al., 2019), a large and important mining area in the northern part of Zambia (Aurélien et al., 2022; Martinez-Alonso et al., 2023; Kříbek et al., 2023). Sracek (2015) found various associations of Fe with Cu, Co, Pb, V, As, Pb, and Zn for mines in Zambia and Namibia, characterized by different climates and ages of the core. At a receptor site on the Zambian Copperbelt in Zimbabwe, the analysis by Nyanganyura et al. (2007) identified the mixing of mineral dust and metal smelting emissions by distinguishing the long-range transport of a aerosols containing Fe, Al, Si but also Co from a non-ferrous smelter component contributing to the fine aerosol

https://doi.org/10.5194/egusphere-2025-446
Preprint. Discussion started: 8 April 2025

fraction only, and characterized by S, Zn, As, and Pb. Ettler et al. (2007) indicated that iron is enriched both with respect to Al and Si in dust liberated from Cu–Co metal smelters in the Zambian Copperbelt. However, Meter et al. (1999) showed that enrichment is variable on an event basis depending on the pyro-metallurgical processing of ores and their composition.

We henceforth conclude that during P1 and P2 the aerosol composition was dominated by natural Namibian mineral dust sources with a composition very similar to the average dust composition measured at the same site in 2016-2017 (Klopper et al., 2020) and reaching the site within the southerly air flow. Conversely, during the last part of P3, the dust reaching Henties Bay was fugitive material from anthropogenic activities. The air masses during the second part of P3 could originate as far as from the Zambian Copper belt.

These conclusions are further corroborated by the CAMS reanalysis shown in Figure S7 in the supplementary material. During P1 and P2 the dust mass mixing ratio reached up to 120 µg m^{-3} (100 µg kg^{-1} on the CAMS map) at the surface in correspondence with the coastal sources in Namibia as a response to the prevailing south-easterly winds (Figure S4) dominating the near-surface circulation from 23 August to 3 September. Continental dust sources were activated on 22 August and 1 September, in association with south-westerly near-surface winds, and on 28-29 August and 4-5 September, in association with near surface convergence of south-westerly and north-easterly winds. From 6 September onwards, no remarkable dust activity was observed, while the circulation had changed (Figure S7). The CAMS reanalysis also showed that the sulphate mixing ratios at the surface reached 6 µg m^{-3} (5 µg kg^{-1} on the CAMS map) in the Zambian Copper Belt and in the urban area of Pretoria and Johannesburg (Figure S7), also a known pollution hotspot (Martinez-Alonso et al., 2023). Sulphate aerosols remained close to their source regions until the end P2. With the installation of the continental high on the 3 September, sulphate aerosols were recirculated south-westwards towards Henties Bay during P3, in particular during 10-12 September.

3.3 Iron mineralogy

The first derivative of the four XANES normalized spectra corresponding to the highest Fe concentrations measured during AEROCLO-sA are shown in Figure 5. The remaining spectra, including those of the standard minerals and compounds used for the deconvolution, are reported in Figure S8.

https://doi.org/10.5194/egusphere-2025-446
Preprint. Discussion started: 8 April 2025

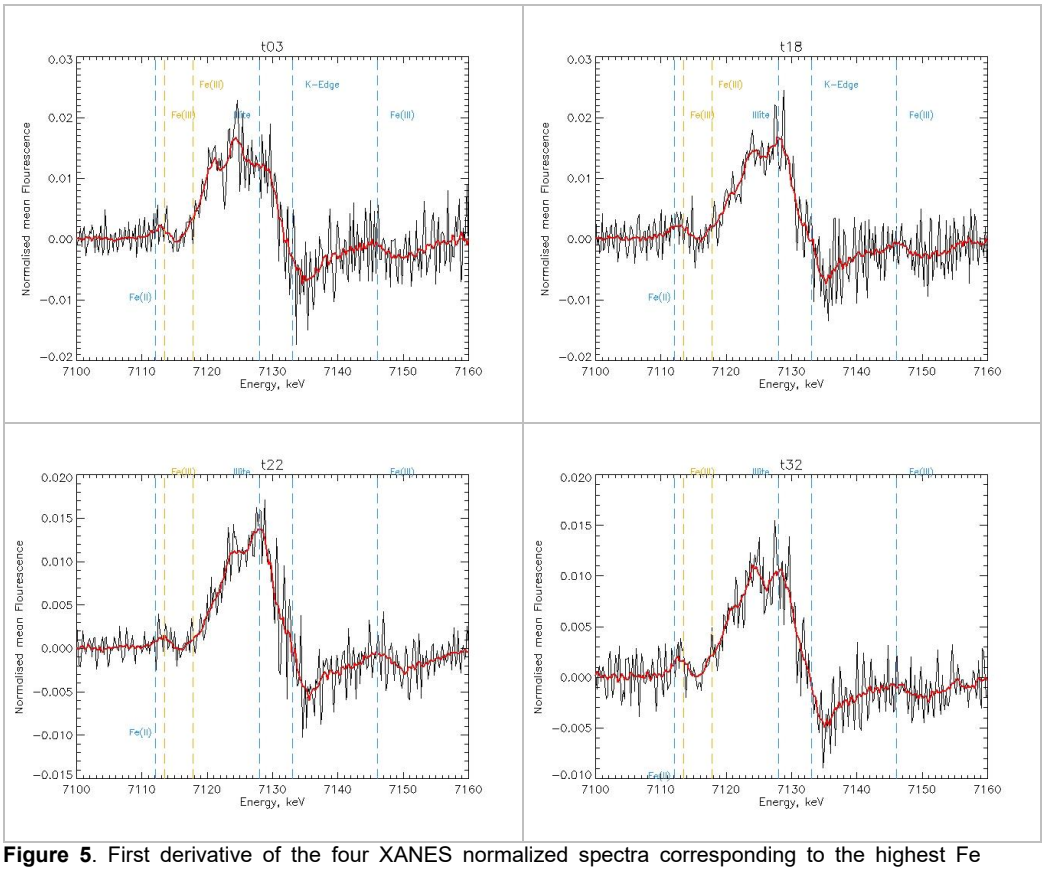

Figure 5. First derivative of the four XANES normalized spectra corresponding to the highest Fe concentrations measured during AEROCLO-sA (see Table S3). The spectral positions of the absorption bands of Fe(II) and Fe(III) in the pre-edge region (7112.1 to 7117.8 eV) as well as those of illite (7128 eV) and various Fe(III) minerals, including hematite (7146 eV), according to Wilke et al. (2001) are indicated by vertical intermittent lines.

Because of the small quantities of particle mass collected on the filters, the XANES spectra are rather noisy. The main features can nevertheless be explored after smoothing. They all are rather similar. In the region between 7122 and 7128 eV, two to three peaks are present with different intensities depending on the sample. The peak at 7128 eV is minor on sample T03 (P1 period) for which the peaks at 7122 and 7126 eV dominate. The peak at 7122 eV is not present afterwards. For samples T18 and T22 in the P2 and beginning of P3 periods, only the peaks at 7126 and 7128 eV are present, the intensity of the latter being higher than the one of the former, while those peaks have equal intensity on sample T032 in the P3 period. For mineral dust from northern Africa, Formenti et al. (2014) showed that the relative proportions of these peaks can be related to the type of clays, but also to the presence of iron oxides in the form of hematite (Fe_2O_3) or goethite (FeOOH). Peaks between 7132 and 7136 eV are distinctive of clays and iron oxides in the form of hematite, but are not present for

https://doi.org/10.5194/egusphere-2025-446
Preprint. Discussion started: 8 April 2025

goethite. In our samples, a minor shoulder in this spectral region is observed only for a few samples (T24, T25, and T31) collected in September. On the other hand, the pre-edge region between 7110 and 7116 eV is sensitive to the iron oxidation state. The majority of our samples seem to peak around 7113-7114 eV, indicating that iron is predominantly in the Fe(III) oxidation state. Only for a few samples (T10, T25, T26, T30, and T37), the pre-edge peak is closer to 7112 eV indicating that Fe(II) could be the predominant oxidation state.

Several attempts of least square reduction were done with a variable number of references to reflect the many mineralogical forms in which iron can be found and verify the stability of the solution. While the relative proportions might have changed by a few percent, the overall repartition was found to be consistent and independent of the selected references.

The average least-square apportionment of the total TSP elemental iron is presented in Table 1 in terms of the mean fractions par sampling period and mineralogical classes.

Table 1. Apportionment of total iron (percent mean and standard deviation) by the least-square deconvolution of the XANES spectra obtained on the filter samples indicated in the first row. Results are grouped by period and by mineral classes.

	21-31 Aug 2017 T01-T14	1-2 Sep 2017 T15-T18	2-7 Sep 2017 T20-T27	8-12 Sep 2017 T28-T38
Clays	49 ± 13	58 ± 12	53 ± 11	42 ± 10
Iron oxides	40 ± 10	36 ± 8	40 ± 9	46 ± 8
Oxalate	4 ± 4	3 ± 4	3 ± 4	5 ± 7
Pyrite	7 ± 5	3 ± 4	4 ± 5	7 ± 4

The largest contribution to the total iron is by clays, between 42 to 58%, with illite and montmorillonite contributing in equal proportions. While a clear temporal trend cannot be defined, the contribution of clays is lowest during the latest sampling period (6-12 September 2017). The second largest contribution is by iron oxides, accounting for between 38 to 45% of the total iron throughout the sampling period. The contribution of FeO, iron oxide in Fe(II) form, is low and extremely variable from sample to sample and not necessarily retrieved for samples in which a shift towards the Fe(II) seems evident in the pre-edge region (T10, T25, T26, T30, and T37). The period P3 is also characterized by the lowest contribution of Fe(III) oxide (64% vs 72-75%). Ferrihydrite (14 ± 7% of total iron) and goethite (8 ± 6% of total iron) showed their highest contributions during P2 (21% and 12% respectively), while hematite (8 ± 6 of total iron) was highest in September (P3). Sracek (2015) found that the formation of secondary hematite is favoured by tropical climate conditions in mines in Zambia compared to Namibia. In contrast to northern African dust, the least-square reduction shows that the presence of magnetite is significant in the dust collected during the campaign, contributing 10-15% to the total iron oxide fraction. Magnetite can be found in sediments in the Erongo region of coastal Namibia

https://doi.org/10.5194/egusphere-2025-446
Preprint. Discussion started: 8 April 2025

(Lohmeier et al. 2021), but also in anthropogenic emissions, such as for example those from metal smelting (Rathod et al. 2020). Zhang et al. (2022) investigated the light-absorbing properties and single particle composition from airborne measurements offshore central Africa during the ORACLES 2018 campaign, and attributed the presence of magnetite to the high-temperature conversion of hematite and/or goethite in biomass-burning plumes or to industrial or vehicular emissions, including from pyro-metallurgical processing in the Zambian Copperbelt. Pyrite (FeS) and Fe-oxalate complexes were also detected throughout the campaign, by their average contribution was extremely low, with the exceptions of 28-29 August 2017 (T10, approximately 19%) and 11 September (T35-36, approximately 30%).

3.4 Iron solubility

Figure 6 presents the time series of the fractional solubility for Al, Si and Fe, as well as those of fluoride (F^-) and MSA measured in the TSP fraction during the field campaign.

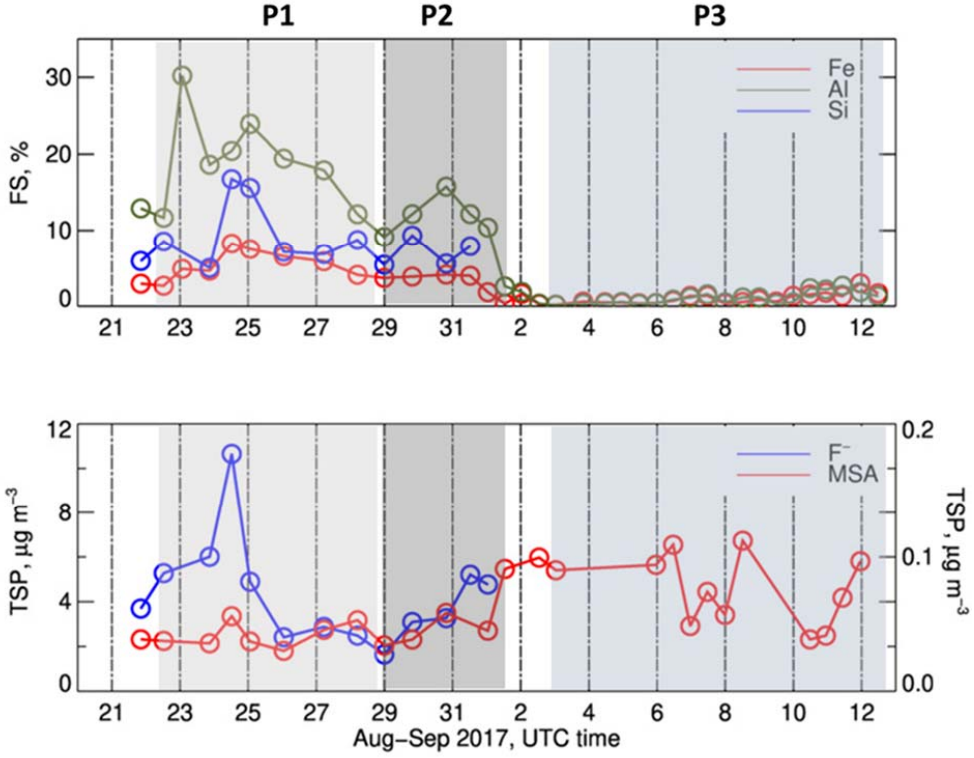

Figure 6. Top panel: Time series of the fractional solubility Al, Si and Fe in the TSP fraction. Bottom panel: Time series of concentrations of F^- (blue) and MSA (red) in the TSP fraction. The MSA concentrations are reported on the right axis of lower panel.

https://doi.org/10.5194/egusphere-2025-446
Preprint. Discussion started: 8 April 2025

During P1 and P2, the fractional solubility was measurable and of the order of 2-8% for Fe, 9-24% for Al, 5-17% for Si and 1.5-4% for Ti (not shown). After that, during P3, their fractional solubility drastically dropped to 0.2-1.7% for Fe and 0.2-2.6% for Al, whereas the fractional solubility of Si and Ti was not measurable (dissolved concentrations under limit of detection). A similar behaviour was observed for most of the measured trace metals (As, Co, Cr, Cu, Ni, Pb, Ti, and Zn, Figure S9).

The percent fractional solubility of iron measured during P1 and P2 was of the same order of magnitude as the lowest solubility values reported at the same sampling site for PM_{10} dust particles by Desboeufs et al. (2024) for the period April to December 2017, when values as high as 20% were measured when MSA in the particle phase was most concentrated. These authors attributed the enhanced solubility to processing (photo-reduction) of the dust by gas-phase dimethyl sulphide (DMS) emitted by the coastal Benguela upwelling. In the present dataset, this association cannot be made. Figure 6 shows that the MSA concentrations were of the same order of magnitude throughout the campaign, and actually slightly more concentrated during P2 and P3, when, on the other hand, the Fe fractional solubility was the lowest. Soluble Fe was also not correlated with oxalate (Pearson correlation coefficient r ~ 0.3), another renown organic ligands (Paris and Desboeufs, 2013).

On the other hand, Figure 6 shows that during P1 and P2, the temporal variability of the fractional solubility of Al, Si and Fe closely followed that of the mass concentration of fluoride (correlation coefficient of 0.87, 0.85 and 0.81, respectively). Fluoride has been identified to be a good ligand of metals in aqueous solution, notably Fe(III) in comparison to Fe(II) (Connick et al., 1956; Bond and Hefter, 1980). The abundance of fluoride ions could act to facilitate the metal complexation on the particle surfaces, potentially promoting their release from the bulk oxide and dissolution at the solid/liquid interface (Arnesen et al., 1998; Tao et al., 2022). In particular, F^- may contribute to the disruption of the Si-O lattice bond by forming SiF_6^{2-} complexes at acidic pH (Mitra and Rimstidt, 2009).

4 Conclusive remarks

The three weeks of aerosol sampling at the Henties Bay coastal site in Namibia during the AEROCLO-sA field campaign coincided with a transition period between two synoptic regimes: the dominance of southerly air flow, associated with the reinforcement of the South Atlantic anticyclone (22 to 31 August 2017) and the dominance of north-easterly air flow (1 to 12 September 2017), associated with the installation of the mid-tropospheric continental high. Those synoptic regimes corresponded to a significant change in the aerosol composition measured at the site and in particular of that of mineral dust. During August and the first few days of September, the dust was natural windblown from the southerly gravel plains with a

https://doi.org/10.5194/egusphere-2025-446
Preprint. Discussion started: 8 April 2025

composition consistent with that previously found in Namibia (Klopper et al., 2020). Gater, the dust was fugitive from anthropogenic mining and possibly also from smelting emissions as far as in the Zambian Copper Belt. The anthropogenic influence in the latter part of the campaign was also documented by the composition of the organic aerosol, which was rich in highly unsaturated compounds as well as saturated N-containing compounds in the latter two periods, more typical of anthropogenic pollution. A second major difference in the composition of the air masses was the high fluoride content until September 2 attributed to emissions from the marine shelf south of Henties Bay.

Taking advantage of those differences, this paper presents the first case study analysis of differences and similarities in the composition of natural and anthropogenic dust, with two key findings: (1) the elemental composition of the anthropogenic dust is enriched in silicon and heavy metals, notably As, Mn, Cu, Cd, Pb, and Zn, and depleted in Al; (2) metals in anthropogenic dust are less water-soluble than in the natural aeolian dust. In particular, the fractional solubility of iron in the natural dust ranged between 2 and 8%, but remained lower than 2% in the anthropogenic dust. This is rather unexpected when taking into account the current literature on anthropogenic dust influenced by combustion, reporting that the iron solubility would be the order of 50% (e.g., Li et al., 2017; Ueda et al., 2023). There are various possible explanations to this fact. First of all, the mineralogy of iron. The most soluble form, ferrihydrite (Journet et al., 2008; Shi et al., 2012), was more abundant in the natural dust, while the less soluble forms of iron (iron oxides such as hematite and magnetite) were more frequent in the fugitive dust, which conversely, could be more efficient in absorbing light at short wavelengths. Secondly, during the first part of the campaign, the aerosol particles were smaller in size, which is known to promote particle solubility, both directly but also in an indirect way, allowing more intense atmospheric processing (Hamilton et al., 2022). Thirdly, our results indicate in a very clear way the extent of which the solubility of iron is linked to the abundance of fluoride ions during the first part of the campaign. While we do not have insights in the mineralogical forms of the metals other than iron, the similar behaviour of their dissolved concentrations, in particular Al and Si, suggest that the marine emissions of fluoride from the Benguela shelf could play a key role in sustaining the complexation of metals dust particles and facilitate their dissolution, supplementing the processing by DMS described for iron in Desboeufs et al. (2024). Such high concentrations of F^- ions are not only unexpected but also they open questions for further studies in this environment. Similarly, to what is known for chloride or bromine (Finlayson-Pitts, 2010, Simpson et al., 2015) one cannot exclude recycling F^- into reactive fluorinated radicals through heterogeneous processes. This call for further targeted reanalysis of the organic matter sampled during this campaign both the gaseous and particulate phases and for further laboratory work to investigate this quite poorly know

https://doi.org/10.5194/egusphere-2025-446
Preprint. Discussion started: 8 April 2025

chemistry. Finally, our results suggest that, in the absence of processing by DMS or oceanic fluoride, the transport of mining dust, including from the Zambian Copper Belt, is unlikely to be a significant source of dissolved iron, but also of elements such as Mn, Cu and Zn, which are toxic to phytoplankton even at low concentrations, and if assimilated, could alter the oceanic productivity and microbial biogeochemistry (Adriano, 2001; Jordi et al., 2012; Mahowald et al., 2018; Yang et al. 2019).

Future work should expand these results by addressing the frequency and intensity of those occurrences on a longer time scale, as well as the mineralogy of metals and their processing by marine emissions in the laboratory.

https://doi.org/10.5194/egusphere-2025-446
Preprint. Discussion started: 8 April 2025

Data Availability. All data are made freely available by the French national service for atmospheric data AERIS-SEDOO data at https://baobab.sedoo.fr/AEROCLO/.

Code Availability. The FASTOSH XANES data analysis package is available for download at https://www.synchrotron-soleil.fr/fr/lignes-de-lumiere/samba (last accessed: 02/03/2024).

Author contribution. PF coordinated the AEROCLO-sA project and funding, led the field campaign and the data analysis, and wrote the manuscript with contributions from all the co-authors. SM performed PMF analysis. AZ performed ESI-HRMS analysis and analysed data. CG collected samples, supervised PMF and ESI-HRMS analyses and their data interpretation. CB contributed to the interpretation of the dust solubility and composition. KD analysed the fractional solubility measurements. MG analysed CAMS reanalysis. GS performed back-trajectories calculations. SC performed XRF analysis, ST performed IC / ICP analysis, FB and CDB performed XANES measurements under the supervision of GL. AF, JFD, AN and SJP participated and facilitated the field campaign.

Special issue statement. This article is part of the special issue “New observations and related modelling studies of the aerosol–cloud–climate system in the Southeast Atlantic and southern Africa regions (ACP/AMT inter-journal SI)”. It is not associated with a conference.

Competing interests. Some authors are members of the editorial board of journal ACP.

Acknowledgements

Authors are grateful to the AEROCLO-sA consortium for their work in the field and during the preparation of the field campaign, and SANUMARC for hosting the field campaign. The authors wish to thank AERIS (https://www.aeris-data.fr/), the French center for atmospheric data and service, for providing the campaign website and organizing the curation and open distribution of AEROCLO-sA data.

Funding support

This work was supported by the French National Research Agency under grant agreement n° ANR-15-CE01-0014-01, the French national program LEFE/INSU, the French National Agency for Space Studies (CNES), and the South African National Research Foundation (NRF) under grant UID 105958. CG’s work was supported by the Supporting TAlent in ReSearch@University of Padova STARS-StG “MOCAA”, and a BP Next Generation fellowship awarded by the Yusuf Hamied Department of Chemistry at the University of Cambridge. This research received additional resources through the “The role of Secondary Organic Aerosols on the climate over the west coast of southern Africa (SOA-Clim)”, International Research Project supported by University of Cambridge and CNRS. MG was supported by the project “Dipartimento di Eccellenza 2023–2027”, funded by the Italian Ministry of Education, University and Research at IUSS Pavia. The PEGASUS facility receives funding as a national facility (instrument national) of the CNRS INSU.

https://doi.org/10.5194/egusphere-2025-446
Preprint. Discussion started: 8 April 2025

References

Adebiyi, A., Kok, J. F., Murray, B. J., Ryder, C. L., Stuut, J.-B. W., Kahn, R. A., Knippertz, P., Formenti, P., Mahowald, N. M., Pérez García-Pando, C., Klose, M., Ansmann, A., Samset, B. H., Ito, A., Balkanski, Y., Di Biagio, C., Romanias, M. N., Huang, Y., and Meng, J.: A review of coarse mineral dust in the Earth system, Aeol. Res., 60, 100849, https://doi.org/10.1016/j.aeolia.2022.100849, 2023.

Adriano, D.C., Trace elements in terrestrial environments: biogeochemistry, bioavailability, and risks of metals. 2nd ed. New York Berlin Heidelberg: Springer, https://doi.org/10.1007/978-0-387-21510-5, 2001.

Arnesen, A. K. M.: Effect of fluoride pollution on pH and solubility of Al, Fe, Ca, Mg, K and organic matter in soil from Ardal (Western Norway), Water. Air. Soil Pollut., 103(1–4), 375–388, doi:10.1023/A:1004921600022, 1998.

Aurélien, N. , Ousmane, S. and Pitiya, R., Zambia's Copperbelt Area and Copper Mining: A Review. J. Geosci. Environ. Protection, 10, 67-75. doi: 10.4236/gep.2022.103005, 2022.

Bikkina, P., Kawamura, K., Bikkina, S., Kunwar, B., Tanaka, K., and Suzuki, K.: Hydroxy Fatty Acids in Remote Marine Aerosols over the Pacific Ocean: Impact of Biological Activity and Wind Speed, ACS Earth and Space Chemistry, 3, 366-379, 10.1021/acsearthspacechem.8b00161, 2019.

Bond, A. M. And Hefter, G. T. (Eds.): Critical Survey of Stability Constants and Related Thermodynamic Data of Fluoride Complexes in Aqueous Solution, Pergamon, ii, https://doi.org/10.1016/B978-0-08-022377-3.50001-6, 1980.

Caponi, L., Formenti, P., Massabó, D., Di Biagio, C., Cazaunau, M., Pangui, E., Chevaillier, S., Landrot, G., Andreae, M. O., Kandler, K., Piketh, S., Saeed, T., Seibert, D., Williams, E., Balkanski, Y., Prati, P., and Doussin, J.-F.: Spectral- and size-resolved mass absorption efficiency of mineral dust aerosols in the shortwave spectrum: a simulation chamber study, Atmos. Chem. Phys., 17, 7175-7191, https://doi.org/10.5194/acp-17-7175-2017, 2017.

Cavalli, F., Viana, M., Yttri, K. E., Genberg, J. and Putaud, J.-P.: Toward a standardised thermal-optical protocol for measuring atmospheric organic and elemental carbon: the EUSAAR protocol, Atmos. Meas. Tech., 3(1), 79–89, doi:10.5194/amt-3-79-2010, 2010.

Compton, J. S., and Bergh, E. W.: Phosphorite deposits on the Namibian shelf, Marine Geology, 380, 290-314, https://doi.org/10.1016/j.margeo.2016.04.006, 2016.

Connick, R. E., Hepler, L. G., Hugus, Z. Z. Jr., Kury, J. W., Latimer, W. M., and Tsao, M.-S.: The Complexing of Iron(III) by Fluoride Ions in Aqueous Solution: Free Energies, Heats and Entropies, J. Am. Chem. Soc., 78, 1827–1829, https://doi.org/10.1021/ja01590a015, 1956.

Desboeufs, K., Formenti, P., Torres-Sánchez, R., Schepanski, K., Chaboureau, J.-P., Andersen, H., Cermak, J., Feuerstein, S., Laurent, B., Klopper, D., Namwoonde, A., Cazaunau, M., Chevaillier, S., Feron, A., Mirande-Bret, C., Triquet, S., and Piketh, S. J.: Fractional solubility of iron in mineral dust aerosols over coastal Namibia: a link to marine biogenic emissions?, Atmos. Chem. Phys., 24, 1525–1541, https://doi.org/10.5194/acp-24-1525-2024, 2024.

Ettler, V., Mihaljevič, M., Kříbek, B., Majer, V., and Šebek, O.: Tracing the spatial distribution and mobility of metal/metalloid contaminants in Oxisols in the vicinity of the Nkana copper smelter, Copperbelt province, Zambia, Geoderma, 164, 73-84, https://doi.org/10.1016/j.geoderma.2011.05.014, 2011.

Ettler, V., Vítková, M., Mihaljevič, M., Šebek, O., Klementová, M., Veselovský, F., Vybíral, P., and Kříbek, B.: Dust from Zambian smelters: mineralogy and contaminant bioaccessibility, Environmental Geochemistry and Health, 36, 919-933, 10.1007/s10653-014-9609-4, 2014.

https://doi.org/10.5194/egusphere-2025-446
Preprint. Discussion started: 8 April 2025

Finlayson-Pitts, B., Halogens in the troposphere, Anal. Chem., 82, 3, 770–776, https://doi.org/10.1021/ac901478p, 2010.

Flamant, C., Gaetani, M., Chaboureau, J.-P., Chazette, P., Cuesta, J., Piketh, S. J., and Formenti, P.: Smoke in the river: an Aerosols, Radiation and Clouds in southern Africa (AEROCLO-sA) case study, Atmos. Chem. Phys., 22, 5701–5724, https://doi.org/10.5194/acp-22-5701-2022, 2022.

Formenti, P., S. Nava, P. Prati, S. Chevaillier, A. Klaver, S. Lafon, F. Mazzei, G. Calzolai, and M. Chiari, Self-attenuation artifacts and correction factors of light element measurements by X-ray analysis: Implication for mineral dust composition studies, J. Geophys. Res., 115, D01203, doi:10.1029/2009JD012701, 2010.

Formenti, P., S. Caquineau, S. Chevaillier, A. Klaver, K. Desboeufs, J. L. Rajot, S. Belin and V. Briois, Dominance of goethite over hematite in iron oxides of mineral dust from Western Africa: quantitative partitioning by X-ray absorption spectroscopy, J. Geophys. Res., 119, 12740-1275, 2014.

Formenti, P., D'Anna, B., Flamant, C., Mallet, M., Piketh, S. J., Schepanski, K., Waquet, F., Auriol, F., Brogniez, G., Burnet, F., Chaboureau, J.-P., Chauvigné, A., Chazette, P., Denjean, C., Desboeufs, K., Doussin, J.-F., Elguindi, N., Feuerstein, S., Gaetani, M., Giorio, C., Klopper, D., Mallet, M. D., Nabat, P., Monod, A., Solmon, F., Namwoonde, A., Chikwililwa, C., Mushi, R., Welton, E. J. and Holben, B.: The Aerosols, Radiation and Clouds in Southern Africa Field Campaign in Namibia: Overview, Illustrative Observations, and Way Forward, Bull. Am. Meteorol. Soc., 100(7), 1277–1298, doi:10.1175/BAMS-D-17-0278.1, 2019.

Frossard, A. A., Russell, L. M., Burrows, S. M., Elliott, S. M., Bates, T. S., and Quinn, P. K.: Sources and composition of submicron organic mass in marine aerosol particles, J. Geophys. Res, 119, 12,977-913,003, https://doi.org/10.1002/2014JD021913, 2014.

Fuge, R.: Fluorine in the environment, a review of its sources and geochemistry, Appl. Geochemistry, 100, 393–406, doi:10.1016/j.apgeochem.2018.12.016, 2019.

Gaetani, M., Pohl, B., Alvarez Castro, M. C., Flamant, C., and Formenti, P.: A weather regime characterisation of winter biomass aerosol transport from southern Africa, Atmos. Chem. Phys., 21, 16575–16591, https://doi.org/10.5194/acp-21-16575-2021, 2021.

Giorio, C., Doussin, J. F., D'Anna, B., Mas, S., Filippi, D., Denjean, C., Mallet, M. D., Bourrianne, T., Burnet, F., Cazaunau, M., Chikwililwa, C., Desboeufs, K., Feron, A., Michoud, V., Namwoonde, A., Andreae, M. O., Piketh, S. J. and Formenti, P.: Butene Emissions From Coastal Ecosystems May Contribute to New Particle Formation, Geophys. Res. Lett., 49(10), doi:10.1029/2022GL098770, 2022.

Hamilton, D. S., Perron, M. M. G., Bond, T. C., Bowie, A. R., Buchholz, R. R., Guieu, C., Ito, A., Maenhaut, W., Myriokefalitakis, S., Olgun, N., Rathod, S. D., Schepanski, K., Tagliabue, A., Wagner, R., and Mahowald, N. M.: Earth, Wind, Fire, and Pollution: Aerosol Nutrient Sources and Impacts on Ocean Biogeochemistry, Annual Review of Marine Science, 14, 303–330, https://doi.org/10.1146/annurev-marine-031921-013612, 2022.

Heine, K. and Völkel, J., Clay Minerals in Namibia and their Significance for the Terrestrial and Marine Past Global Change Research, African Study Monographs. Supplementary Issue., 40, 31-50, publisher The Research Committee for African Area Studies, Kyoto University, 2010.

Inness, A., Ades, M., Agustí-Panareda, A., Barré, J., Benedictow, A., Blechschmidt, A.-M., Dominguez, J. J., Engelen, R., Eskes, H., Flemming, J., Huijnen, V., Jones, L., Kipling, Z., Massart, S., Parrington, M., Peuch, V.-H., Razinger, M., Remy, S., Schulz, M., and Suttie, M.: The CAMS reanalysis of atmospheric composition, Atmos. Chem. Phys., 19, 3515–3556, https://doi.org/10.5194/acp-19-3515-2019, 2019.

Klopper, D., Formenti, P., Namwoonde, A., Cazaunau, M., Chevaillier, S., Feron, A., Gaimoz, C., Hease, P., Lahmidi, F., Mirande-Bret, C., Triquet, S., Zeng, Z. and Piketh, S. J.: Chemical

https://doi.org/10.5194/egusphere-2025-446
Preprint. Discussion started: 8 April 2025

composition and source apportionment of atmospheric aerosols on the Namibian coast, Atmos. Chem. Phys., 20(24), 15811–15833, doi:10.5194/acp-20-15811-2020, 2020.

Kříbek, B., Nyambe, I., Sracek, O., Mihaljevič, M., and Knésl, I.: Impact of Mining and Ore Processing on Soil, Drainage and Vegetation in the Zambian Copperbelt Mining Districts: A Review, Minerals, 13, 384, doi:10.3390/min13030384, 2023.

Jordi, A., Basterretxea, G., Tovar-Sánchez, A., Alastuey, A., and Querol, X.: Copper aerosols inhibit phytoplankton growth in the Mediterranean Sea, Proc. Nat. Acad. Sci., 109, 21246-21249, doi:10.1073/pnas.1207567110, 2012.

Journet, E., K. Desboeufs, S. Caquineau, & J.L. Colin, Mineralogy as a critical factor of dust iron solubility, Geophys. Res. Letters, 35, doi:10.1029/2007GL031589, 2008.

Li, W., Xu, L., Liu, X., Zhang, J., Lin, Y., Yao, X., Gao, H., Zhang, D., Chen, J., Wang, W., Harrison, R. M., Zhang, X., Shao, L., Fu, P., Nenes, A., and Shi, Z.: Air pollution – aerosol interactions produce more bioavailable iron for ocean ecosystems, Sci. Adv., 3, e1601749, https://doi.org/10.1126/sciadv.1601749, 2017.

Liebenberg-Enslin, H., von Oertzen, D., and Mwananawa, N.: Dust and radon levels on the west coast of Namibia – What did we learn?, Atmos. Poll. Res., 11, 2100-2109, https://doi.org/10.1016/j.apr.2020.05.020, 2020.

Lohmeier, S., B. G. Lottermoser, K. Strauß, T. Adolffs, S. Sindern, D. Gallhofer, Nearshore marine garnet and magnetite placers in the Erongo and S-Kunene regions, Namibia, Journal of African Earth Sciences, 180, 104221, https://doi.org/10.1016/j.jafrearsci.2021.104221, 2021.

Mahowald, N.M., D. S. Hamilton, K., R. M. Mackey, J. K. Moore, A. R. Baker, R. A. Scanza, and Y. Zhang, Aerosol trace metal leaching and impacts on marine microorganisms, Nat. Commun., 5, 9, 2614, 10.1038/s41467-018-04970-7, 2018.

Mänd, K., Kirsimäe, K., Lepland, A., Crosby, C., Bailey, J., Konhauser, K., Wirth, R., Schreiber, A., and Lumiste, K.: Authigenesis of biomorphic apatite particles from Benguela upwelling zone sediments off Namibia: The role of organic matter in sedimentary apatite nucleation and growth, Geobiology, 16, 10.1111/gbi.12309, 2018.

Martínez-Alonso, S., Veefkind, J. P., Dix, B., Gaubert, B., Theys, N., Granier, C., et al., S-5P/TROPOMI-derived NOx emissions from copper/cobalt mining and other industrial activities in the Copperbelt (Democratic Republic of Congo and Zambia). Geophys. Res. Lett., 50, e2023GL104109. https://doi.org/10.1029/2023GL104109, 2023.

Meter, S. L., P. Formenti, S. J. Piketh, H. J. Annegarn, and M. A. Kneen, PIXE investigation of aerosol composition in the Zambian Copperbelt, Nucl. Inst. and Meth., B150, 433–438, 1999.

Micella, I., Kroeze, C., Bak, M. P., and Strokal, M.: Causes of coastal waters pollution with nutrients, chemicals and plastics worldwide, Marine Pollution Bulletin, 198, 115902, https://doi.org/10.1016/j.marpolbul.2023.115902, 2024.

Michalowicz, A., Moscovici, J., Muller-Bouvet, D., and Provost, K.: MAX: Multiplatform Applications for XAFS, Journal of Physics Conference Series (Online), 190, 4, Doi:101088/1742-6596/190/1/012034, 2009.

Mileusnić, M., Mapani, B. S., Kamona, A. F., Ružičić, S., Mapaure, I., and Chimwamurombe, P. M.: Assessment of agricultural soil contamination by potentially toxic metals dispersed from improperly disposed tailings, Kombat mine, Namibia, J. Geochemical Exploration, 144, 409-420, https://doi.org/10.1016/j.gexplo.2014.01.009, 2014.

Mitra, A., and Rimstidt, J. D.: Solubility and dissolution rate of silica in acid fluoride solutions, Geochimica et Cosmochimica Acta, 73, 7045-7059, https://doi.org/10.1016/j.gca.2009.08.027, 2009.

https://doi.org/10.5194/egusphere-2025-446
Preprint. Discussion started: 8 April 2025

Mwaanga, P., Silondwa, M., Kasali, G., and Banda, P. M.: Preliminary review of mine air pollution in Zambia, Heliyon, 5, e02485, https://doi.org/10.1016/j.heliyon.2019.e02485, 2019.

Nekhoroshkov, P., Bezuidenhout, J., Zinicovscaia, I., Yushin, N., Vergel, K., and Frontasyeva, M.: Levels of Elements in Typical Mussels from the Southern Coast of Africa (Namibia, South Africa, Mozambique): Safety Aspect, Water, 13, 3238, 2021.

Nyanganyura, D., Maenhaut, W., Mathuthu, M., Makarau, A., and Meixner, F. X.: The chemical composition of tropospheric aerosols and their contributing sources to a continental background site in northern Zimbabwe from 1994 to 2000, Atmos. Environ., 41, 2644-2659, https://doi.org/10.1016/j.atmosenv.2006.11.015, 2007.

Omoregie E., E. C. Vellemu, F. Nashima, B. Mudumbi Samona Brian, G. Liswaniso Gadaffi and K. Shimooshili, Assessment of copper levels along the Namibian marine coastline, GSC Biological and Pharmaceutical Sciences, 7, 48-55, https://doi.org/10.30574/gscbps.2019.7.3.0101, 2019.

Onjefu, S. A., Shaningwa, F., Lusilao, J., Abah, J., Hess, E., and Kwaambwa, H. M.: Assessment of heavy metals pollution in sediment at the Omaruru River basin in Erongo region, Namibia, Environ. Poll. Bioavailability, 32, 187-193, 10.1080/26395940.2020.1842251, 2020.

Onipe, T., Edokpayi, J. N., and Odiyo, J. O.: A review on the potential sources and health implications of fluoride in groundwater of Sub-Saharan Africa, Journal of Environmental Science and Health, Part A, 55, 1078-1093, 10.1080/10934529.2020.1770516, 2020.

Paatero, P., Least squares formulation of robust non-negative factor analysis. Chemometrics and Intelligent Laboratory Systems, 37(1), 23–35. https://doi.org/10.1016/S0169-7439(96)00044-5, 1997.

Paatero, P., and Tapper, U., Positive matrix factorization: A non-negative factor model with optimal utilization of error estimates of data values. Environmetrics, 5(2), 111–126. https://doi.org/10.1002/env.3170050203, 1994

Paris, R. and K. Desboeufs, Effect of atmospheric organic complexation on iron-bearing dust solubility, Atmos. Chem. Phys., 13, 4895–4905, doi:10.5194/acp-13-4895-2013, 2013.

Rakovan J.F., J.M.Hughes, Strontium in the apatite structure: strontian fluorapatite and belovite-(ce), The Canadian Mineralogist, 38 (4), 839–845, doi: 10.2113/gscanmin.38.4.839, 2000.

Rajot, J.-L., P. Formenti, S. Alfaro, K. Desboeufs, S. Chevaillier, B. Chatenet, A. Gaudichet, E. Journet, B. Marticorena, S. Triquet, A. Maman, N. Mouget, and A. Zakou, AMMA dust experiment: An overview of measurements performed during the dry season special observation period (SOP0) at the Banizoumbou (Niger) supersite, J. Geophys. Res., doi:10.1029/2008JD009906, 2008.

Rathod, S. D., Hamilton, D. S., Mahowald, N. M., Klimont, Z., Corbett, J. J., and Bond, T. C.: A Mineralogy-Based Anthropogenic Combustion-Iron Emission Inventory, J. Geophys. Res., 125, e2019JD032114, https://doi.org/10.1029/2019JD032114, 2020.

Simpson, W. R., S. S. Brown, A. Saiz-Lopez, J. A. Thornton, and R. von Glasow, Tropospheric Halogen Chemistry: Sources, Cycling, and Impacts, Chem. Rev., 115, 4035-4062, DOI: 10.1021/cr5006638, 2015.

Skamarock, W. C., Klemp, J. B., Dudhia, J., Gill, D. O., Barker, D., Duda, M. G., Powers, J. G., A Description of the Advanced Research WRF Version 3 (No. NCAR/TN-475+STR). University Corporation for Atmospheric Research. doi:10.5065/D68S4MVH, 2008.

Sracek, O., Wanke, H., Ndakunda, N. N., Mihaljevič, M., and Buzek, F.: Geochemistry and fluoride levels of geothermal springs in Namibia, Journal of Geochemical Exploration, 148, 96-104, https://doi.org/10.1016/j.gexplo.2014.08.012, 2015.

https://doi.org/10.5194/egusphere-2025-446
Preprint. Discussion started: 8 April 2025

Sracek, O.: Formation of secondary hematite and its role in attenuation of contaminants at mine tailings: review and comparison of sites in Zambia and Namibia, Frontiers in Environmental Science, 2, 10.3389/fenvs.2014.00064, 2015.

Strain, E.M.A., Lai R.W.S., White C.A., Piarulli S., Leung K.M.Y., Airoldi L., and O'Brien A., Editorial: Marine Pollution - Emerging Issues and Challenges. Front. Mar. Sci. 9:918984. doi: 10.3389/fmars.2022.918984, 2022.

Sylvanus, O., Kgabi, N., and Taole, S.: Heavy Metal Seasonal Distribution in Shore Sediment Samples along the Coastline of Erongo Region, Western Namibia, European Journal of Scientific Research, 139, 49-63, 2016.

Tao, Y., Ye G, Zhang H, Hu Y, Zuo Q, Wang X, Zhu S, Kang X, Zhang Y, Xiang X, et al. Effect of Fluoride Ions on the Surface Dissolution of Vanadium-Bearing Biotite. Separations. 9, 422, https://doi.org/10.3390/separations9120422, 2022.

Ueda, S., Iwamoto, Y., Taketani, F., Liu, M., and Matsui, H.: Morphological features and water solubility of iron in aged fine aerosol particles over the Indian Ocean, Atmos. Chem. Phys., 23, 10117–10135, https://doi.org/10.5194/acp-23-10117-2023, 2023.

Usher, C. R., Michel, A. E., and Grassian, V. H.: Reactions on Mineral Dust, Chemical Reviews, 103, 4883-4940, 10.1021/cr020657y, 2003.

Yang, T., Chen, Y., Zhou, S., and Li, H.: Impacts of Aerosol Copper on Marine Phytoplankton: A Review, Atmos., 10, 414, https://doi.org/10.3390/atmos10070414, 2019.

White, K., Walden, J., and Gurney, S. D.: Spectral properties, iron oxide content and provenance of Namib dune sands, Geomorphology, 86, 219-229, https://doi.org/10.1016/j.geomorph.2006.08.014, 2007.